Gas-Phase Interaction of CO, CO_2, H_2S, NH_3, NO, NO_2, and SO_2 with $Zn_{12}O_{12}$ and Zn_{24} Atomic Clusters

Doust Mohammadi, Mohsen; Louis, Hitler; Chukwu, Udochukwu G.; Bhowmick, Somnath; Rasaki, Michael E.; Biskos, George

DOI
10.1021/acsomega.3c01177

Publication date
2023

Document Version
Final published version

Published in
ACS Omega

ACS OMEGA

http://pubs.acs.org/journal/acsodf

Article

Gas-Phase Interaction of CO, CO_2, H_2S, NH_3, NO, NO_2, and SO_2 with $Zn_{12}O_{12}$ and Zn_{24} Atomic Clusters

Mohsen Doust Mohammadi,* Hitler Louis, Udochukwu G. Chukwu, Somnath Bhowmick, Michael E. Rasaki, and George Biskos*

Cite This: *ACS Omega* 2023, 8, 20621−20633

Read Online

ACCESS | Metrics & More | Article Recommendations | Supporting Information

ABSTRACT: Atmospheric pollutants pose a high risk to human health, and therefore it is necessary to capture and preferably remove them from ambient air. In this work, we investigate the intermolecular interaction between the pollutants such as CO, CO_2, H_2S, NH_3, NO, NO_2, and SO_2 gases with the Zn_{24} and $Zn_{12}O_{12}$ atomic clusters, using the density functional theory (DFT) at the meta-hybrid functional TPSSh and LANl2Dz basis set. The adsorption energy of these gas molecules on the outer surfaces of both types of clusters has been calculated and found to have a negative value, indicating a strong molecular-cluster interaction. The largest adsorption energy has been observed between SO_2 and the Zn_{24} cluster. In general, the Zn_{24} cluster appears to be more effective for adsorbing SO_2, NO_2, and NO than $Zn_{12}O_{12}$, whereas the latter is preferable for the adsorption of CO, CO_2, H_2S, and NH_3. Frontier molecular orbital (FMO) analysis showed that Zn_{24} exhibits higher stability upon adsorption of NH_3, NO, NO_2, and SO_2, with the adsorption energy falling within the chemisorption range. The $Zn_{12}O_{12}$ cluster shows a characteristic decrease in band gap upon adsorption of CO, H_2S, NO, and NO_2, suggesting an increase in electrical conductivity. Natural bond orbital (NBO) analysis also suggests the presence of strong intermolecular interactions between atomic clusters and the gases. This interaction was recognized to be strong and noncovalent, as determined by noncovalent interaction (NCI) and quantum theory of atoms in molecules (QTAIM) analyses. Overall, our results suggest that both Zn_{24} and $Zn_{12}O_{12}$ clusters are good candidate species for promoting adsorption and, thus, can be employed in different materials and/or systems for enhancing interaction with CO, H_2S, NO, or NO_2.

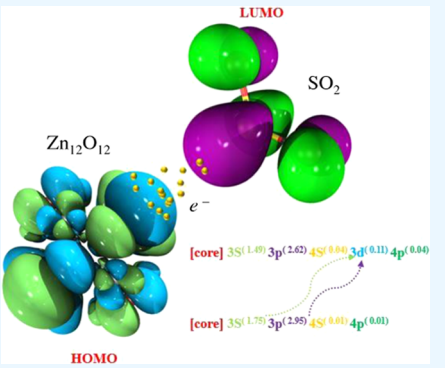

1. INTRODUCTION

Gaseous species in the atmosphere can have adverse effects on human health and climate. CO, for instance, is frequently referred to as a "silent killer" because it can lead to hypoxic damage of tissues at low concentrations, while it can be fatal at high levels.[1] Other gaseous species, including H_2S, NH_3, NO, NO_2, and SO_2, that are emitted by human activities into the atmosphere, can have similar environmental impacts.[2−6] Apart from the effects on human health, certain gaseous species can affect the Earth's climate. CO_2, for instance, is a greenhouse gas that contributes significantly to global warming.[7] Monitoring and regulating the concentrations of specific gaseous species in the atmospheric environment is, therefore, of major necessity for evaluating their potential adverse effects and for implementing effective mitigation strategies.[8]

An extensive range of observational networks to determine the concentration of air pollutants are already available and employed for regulatory purposes.[9] These networks, however, due to their high installation and operational costs, consist of a small number of stations, even in densely populated areas,[10,11] thus limiting the spatial resolution of observational data they can provide and the ability to link them with exposure assessments. A promising alternative to analytical instruments employed for air-quality monitoring is low-cost gas sensors that rely on the interaction of their sensing materials with the target gases.[10] To this end, great efforts are made to develop materials for a wide range of sensors, including electrochemical[12] and metal oxide semiconductor gas sensors,[13] as well as 2D and 1D materials that exhibit high sensitivity and selectivity toward specified target gases.[14,15] Similar materials have also been used as effective adsorbents for the removal of air pollutants,[16,17] or catalysis for their conversion to less harmful species.[18,19]

One of the frequently used one-dimensional (1D) nanomaterials for gas sensors is Zn_nO_n.[20−22] Such materials, being semi-conductive, have a wide direct energy gap[23] and a high excitation binding energy. From this family of materials, the $Zn_{12}O_{12}$ cluster is a condensed octahedron consisting of eight hexagons and six squares.[24] Earlier studies have employed

Received: February 21, 2023
Accepted: May 22, 2023
Published: May 31, 2023

density functional theory (DFT) to verify the stability and electronic properties of the $Zn_{12}O_{12}$ cluster. Studies have shown that $Zn_{12}O_{12}$ is the smallest stable structure of the Zn_nO_n family,[25,26] and therefore it has attracted the attention of many researchers. Yong et al.[27] employed first-principle calculations to investigate $Zn_{12}O_{12}$ cluster-assembled nanowires and the adsorption performance of environmental gases on such structures. Afshari et al.[28] also used DFT to investigate the electronic sensitivity and adsorption interactions of pristine and doped $Zn_{12}O_{12}$ clusters with transition metals, such as Sc, Ti, V, Cr, Mn, Fe, Co, Ni, and Cu, with ethylene oxide, showing that doped species, and particularly those doped with Cr and V, were highly sensitive to the target gas molecule. Similarly, Salmankhani et al.[29] used DFT to compare BeO and ZnO surfaces and reported that although both are inferior to Ni-decorated graphene sheets, the latter provides a better adsorbent for H_2S. Louis et al.[30] also employed DFT to investigate the ability of doped Zn_{11}-X-O_{12} (X = Ag, Au, Pd, and Pt) to sense serotonin, whereas Mukhlif et al.[31] investigated the interactions of $Zn_{12}O_{12}$ nanoclusters with carbamazepine in order to explore their use for drug detection. Along the same lines, Muz et al.[32] investigated the interaction between CH_4 and CO_2 with zinc oxide clusters and found that $Zn_{12}O_{12}$ provides a highly effective adsorbent. In addition, the catalytic activity of $Zn_{12}O_{12}$ nanoclusters has also been investigated by Esrafili et al.,[26] expanding their potential applications.

In this work, we use DFT to understand the electronic characteristics and the intermolecular interaction between the most common air pollutants (i.e., CO, CO_2, H_2S, NH_3, NO, NO_2, and SO_2) onto the surface of $Zn_{12}O_{12}$ clusters. For comparison purposes, we also investigate the interaction of these gases with the pristine Zn_{24} cluster, for which data are available in the literature.[33] Interestingly, our results show that Zn_{24} can behave as a semiconductor (having a band gap of 0.873 eV) and not as a conductor, which is the case of bulk zinc. We also employ frontier molecular orbital (FMO) analysis to assess the stability, conductivity, and sensing ability of the studied compounds, as well as the natural bond orbital (NBO) analysis to investigate the change in natural electron configuration as well as natural charge consideration for the interaction between the surfaces of the atomic clusters and the gases we investigate here. Total density of state (TDOS) plots are also provided to show the position of frontier molecular orbitals and to study the electron distribution of the molecules, whereas quantum theory of atoms in molecules (QTAIM) analysis is used to determine the interactions between the clusters and the gas molecules and also to define the nature of intermolecular interactions. Noncovalent interaction (NCI) and charge transfer analyses have also been carried out.

2. COMPUTATIONAL DETAILS

2.1. Electronic Structure Calculations. Specific properties of materials can be determined by evaluating their electronic structures using DFT methods.[34] In this work, ground-state geometry optimization has been carried out using TPSSh meta-hybrid functional,[35] i.e., the exchange functional provided by Tao, Perdew, Staroverov, and Scuseria,[36] which is a meta-generalized gradient approximation (GGA) exchange functional. The TPSSh functional has been reported to have good accuracy for geometry optimization and therefore improves DFT calculations;[37−40] hence, the choice to utilize it for this study. Also, the LANl2Dz basis set was employed to optimize the geometry of $Zn_{12}O_{12}$ and Zn_{24} structures. Benchmark studies show that the LANl2Dz basis set can capture well the necessary integration space for transition metals and, more specifically, for zinc.[41−43] To scrutinize the fidelity of TPSSh/Lanl2Dz computations, a plethora of diverse systems underwent evaluation via the TPSSh/SDD and ωB97XD/Lanl2Dz methodologies. By keeping the basis set invariant and modulating the functional, or by preserving the functional while manipulating the basis set, judgments were rendered concerning the accrued adsorption energies. All calculations have been carried out using Gaussian 16.[44] Ground-state geometry optimization has been carried out using TPSSh, i.e., the exchange functional provided by Tao, Perdew, Staroverov, and Scuseria,[36] which is a meta-generalized gradient approximation (GGA) exchange functional. The TPSSh functional, i.e. the exchange functional provided by Tao, Perdew, Staroverov, and Scuseria, which is a meta-generalized gradient approximation (GGA) exchange functional.[37−40] To investigate the electronic properties of the clusters, we used FMO analysis. The variations in the electronic energy and the orbital energies were calculated by the GaussSum 3.0 package.[45] Topological QTAIM analysis[46] was also carried out in order to determine the nature of the interatomic interactions. Pictorial representations of frontier molecular orbital from electronic studies were visualized using Visual Molecular Dynamics (VMD) software.[47] To explore the possibility of the donor−acceptor interactions, we used the NBO 3.1 package, which is embedded in the Gaussian 16 package.[44] The resulting structures were visualized using the Chemcraft 1.6 package.[48]

The adsorption energy, E_{ads}, of the systems resulting from the interactions between the gas molecules and the $Zn_{12}O_{12}$ or the Zn_{24} atomic clusters were calculated as follows

$$E_{ads} = E_{complex} - (E_{gas} + E_{cluster}) \quad (1)$$

Here, $E_{complex}$ corresponds to the energy of the gas/cluster system, E_{gas} is the energy of the isolated gas molecules, and $E_{cluster}$ denotes the energy of the adsorbent, i.e., the $Zn_{12}O_{12}$ or the Zn_{24} clusters. Regarding the basis set superposition error, we have verified that this error is smaller than the value of the zero-point energy correction, and therefore they are not calculated in the present study.

2.2. Natural Bond Orbital Calculations. Electrostatic interactions between atoms can also be explained through the NBO analysis, which provides a convenient means to investigate charge transfer or conjugated interactions in a molecular system.[49] Electron density transfer from the bonding orbitals to the anti-bonding orbital can be identified in this analysis, helping to understand how these interactions contribute to the stability of a molecule.[50,51] In this approach, electron density (ρ) is utilized to determine the shape of the atomic orbital in the molecular environment and bonds.[52,53] The intermolecular hydrogen bonding and charge transfer between Lewis and non-Lewis orbitals can be estimated by the second-order perturbation energy described as[54]

$$E(2) = q_i \frac{F_{i,j}^{\ 2}}{\varepsilon_j - \varepsilon_i} = \Delta E_{i,j}^{\ 2} \quad (2)$$

where ε_i and ε_j are the diagonal elements of the density matrix that denote the orbital energies, q_i is the donor orbital occupancy, $F_{i,j}$ are the off-diagonal Fock matrix elements, and $\Delta E_{i,j}^2$ is the stabilization energy.[55]

https://doi.org/10.1021/acsomega.3c01177
ACS Omega 2023, 8, 20621−20633

The second-order perturbation theory has been one of the most commonly employed methods for estimating bond energy effects, whereas many other types of bond order analysis have been developed to account for the bond property, such as the Mulliken bond order analysis,[56] the Mayer bond order analysis, the multicenter bond analysis, or the Wiberg bond order analysis.[57] The above-mentioned methods are based on different assumptions;[58] therefore, an interpretation of the results should be made with caution. It has been reported that the basis set containing diffuse function provides unreliable results for Mulliken bond orders, whereas the Wiberg bond index (WBI) and the Mayer methods are less sensitive to the basis set. The WBI is the addition of the square of an off-diagonal density matrix element between the atoms, and it is determined as follows[59]

$$\mathrm{WBI} = \sum_{K} P_{jk}^2 = 2P_{jj} - P_{jk}^2 \tag{3}$$

where P_{jk} represents the density matrix element and P_{jj} the changing density in the atomic orbital. There is no significant difference between the net bonding or anti-bonding type of element of the density matrix in the WBI.[60]

2.3. Noncovalent Interaction Calculations. In order to evaluate the contribution of electrostatic and dispersion forces, as well as weak interactions in real space, electron density and its first derivative are required for the noncovalent interaction (NCI) analysis. In this analysis, the reduced density gradient (RDG) function, as well as the sign of the produced $\lambda_2(\mathbf{r})\rho(\mathbf{r})$, where λ_2 and ρ are, respectively, the second eigenvalue of Hessian matrix and electron density, is correlated.[61] RDG is a dimensionless quantity that is connected to the electron density and its first derivative.[62] Weak intermolecular forces such as hydrogen bonding, spatial repulsion, and van der Waals, which can play an important role in the stabilization of the systems, can be identified from the NCI analysis.[63] The RDG can be determined as

$$\mathrm{RDG}_{(\mathrm{R})} = \frac{1}{2(3\pi^2)^{1/2}} \frac{\nabla\rho(\mathbf{r})}{\rho(r)^{4/3}} \tag{4}$$

where $\rho(\mathbf{r})$ is the electron density. Large and negative values of the sign $(\lambda_2)\rho$ signify attractive interactions (such as dipole−dipole or hydrogen bonding), while if the sign $(\lambda_2)\rho$ is large and positive, the interaction is nonbonding.[64] A near-zero value, however, indicates very weak van der Waals interactions. The sign of λ_2 helps to differentiate between bonded ($\lambda_2 < 0$) from nonbonded ($\lambda_2 > 0$) interactions.[65]

2.4. Quantum Theory of Atom in Molecule Calculations. QTAIM analysis provides another powerful methodology to investigate the nature of the interaction between the atoms in a molecule.[51] It can be used to make a topological description of a molecule, as proposed by Bader et al.[66] According to this theory, the points in space where gradient of electron density is equal to zero, i.e., $\nabla\rho(\mathbf{r}) = 0$, are the critical points of the electron density.[67] The critical point could be equivalent to a minimum point, a maximum point, or a saddle point and can be categorized into one of the following: (1) atomic critical point (ACP), which signifies the geometrical position of an atom or nucleus (other than hydrogen) and geometrically represents a local maximum point of electron density in three-dimensional space; (2) bond critical point (BCP), which marks a critical point related to a bond of physical or chemical interaction; BCP is represented by a saddle point with two directions of maximum electron density; (3) ring critical point, which signifies a ring or set of atoms forming a ring. Geometrically, it is a saddle point, with maximum electron density in one dimension and minimum in the other two dimensions; and (4) cage critical point (CCP), which is a local minimum point in all three directions of electron density.[52]

To properly characterize the nature of the interaction, the electron density $\rho(\mathbf{r})$, the Laplacian of the electron density $\nabla^2\rho(\mathbf{r})$, the kinetic energy density $G(\mathbf{r})$, the potential energy density $V(\mathbf{r})$, and $\mathrm{G}(\mathbf{r})/\mathrm{V}(\mathbf{r})$ ratio must be determined.[68] A negative value of $\nabla^2\rho(\mathbf{r})$ at a bond critical point and a large value of $\rho(\mathbf{r})$ indicate a covalent intermolecular interaction.[69] In contrast, if $\nabla^2\rho(\mathbf{r})$ is positive, there is a nonsubstrate closed-shell type of interaction (which includes ionic and van der Waals interactions). It is also worth noting that for covalent bonding, i.e., $\nabla^2\rho(\mathbf{r}) < 0$ and a closed-shell interaction dominates if $\nabla^2\rho(\mathbf{r}) > 0$.[70] According to the virial theorem, the following relationship links $G(\mathbf{r})$, $V(\mathbf{r})$, and $\nabla^2\rho(\mathbf{r})$[71]

$$\frac{1}{4}\nabla^2\rho(\mathbf{r}) = 2G(\mathbf{r}) + V(\mathbf{r}) \tag{5}$$

The mode of interaction can be classified by the balance between $G(\mathbf{r})$ and $V(\mathbf{r})$, hence the ratio of G/|V| ratio provides an appropriate index to indicate the nature of interaction.[72] A purely covalent form of interaction is suggested if this ratio is less than 0.5, and noncovalent interaction if the ratio is greater than 1.

3. RESULTS AND DISCUSSION

3.1. Geometry and Structural Analysis. Figure 1 shows the optimized geometries of the $Zn_{12}O_{12}$ and Zn_{24} atomic

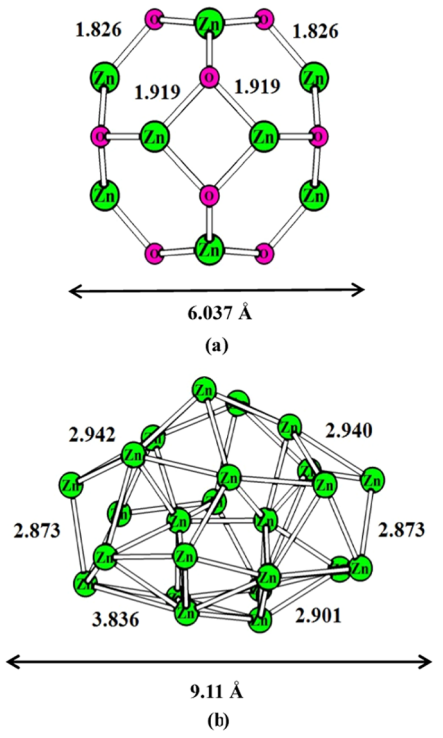

Figure 1. Optimized geometry of (a) $Zn_{12}O_{12}$ and (b) Zn_{24} atomic clusters determined using the meta-hybrid functional TPSSh and LANl2Dz basis set. The bond lengths are expressed in Å.

https://doi.org/10.1021/acsomega.3c01177
ACS Omega 2023, 8, 20621−20633

clusters. To obtain these geometries, we employed ABCluster software[73,74] that uses the artificial bee colony algorithm to find the global minimum structure of a molecular system. As shown by the DFT calculations, the $Zn_{12}O_{12}$ cluster is composed of eight hexagons and six tetragons with T_h symmetry.[75] Structurally, two different Zn−O bonds are observed in the cluster; one is shared by two hexagons with a bond length of 1.826 Å, and the other between a hexagon and a tetragon with a bond length of 1.919 Å. We should note here that the longest distance between atoms in the $Zn_{12}O_{12}$ cluster is 6.037 Å. Due to the relatively high symmetry of this cluster, the number of different positions that can be imagined for the adsorption of gases is limited, as shown in Figure 2. The

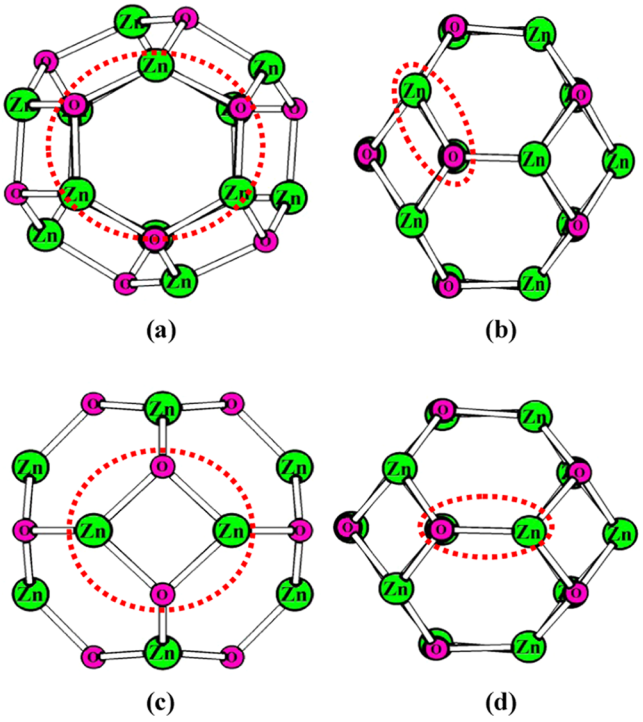

Figure 2. Different adsorption sites (indicated by the regions within the dashed circles) that can be identified in the $Zn_{12}O_{12}$ cluster are (a) in the space surrounded by the hexagonal ring, (b) the bond between the hexagonal ring and the quadrilateral ring, (c) inside the space surrounded by the quadrilateral ring, and (d) the bond between two hexagonal rings.

gas molecules under study can be placed in the vicinity of any Zn or O atoms, whereas the space around the hexagonal or quadrilateral rings can be considered as an adsorption site. We should note here that there are two types of bonds: one between two hexagonal rings and another between the hexagonal or quadrilateral rings. Each of the gases, viz., CO, CO_2, H_2S, NH_3, NO, NO_2, and SO_2, whose optimized geometries are depicted in Figure 3, have been placed in different adsorption sites over these two types of bonds for the geometry optimization calculations. Only the largest adsorption energy found among these sites is reported and discussed in the next section.

In contrast to the $Zn_{12}O_{12}$, the Zn_{24} cluster does not follow any known symmetry (cf. Figure 1b). The two Zn atoms in Zn_{24} are inside a cage surrounded by 22 other atoms. In fact, constructing a cluster with 24 Zn atoms yields a number of different structural isomers that differ in spatial form and total energy. ABCluster software has the ability to examine most of the possible structural isomers and identify the isomer that is more stable than the others in terms of total energy. Different interatomic distances are observed in the Zn_{24} cluster, some of which are shown in Figure 1b for clarity. The size of this cluster is larger than that of $Zn_{12}O_{12}$ (9.11 Å).

Due to the asymmetric structure of Zn_{24}, there are many sites to adsorb the desired gas. Therefore, sampling the adsorption energy in this case is a challenging task in the sense that a much larger number of gas/cluster system candidate structures must be considered for geometry optimization. More specifically, we have generated hundreds of initial configurations of gas-cluster systems that cover the entire space around the cluster that are subsequently used for geometry optimization.

The optimized geometries of the energetically most stable gas-cluster systems are illustrated in Figures 4 and 5 and tabulated in Table S1 in the supporting information (SI). Table 1 provides the intermolecular distances of interacting gas atoms and the two types of clusters we investigated. Close inspection of the bond lengths of each system shows that the longest bond is observed between the two Zn atoms of the $Zn_{12}O_{12}$ cluster and the two O atoms of the NO_2 (2.867 Å) and CO_2 (2.608 Å) molecules. In a similar manner, the shortest bond lengths were observed between the two Zn atoms of the $Zn_{12}O_{12}$ cluster and the S and O atoms of the SO_2 gas molecule (i.e., 1.593 and 1.925 Å, respectively). The other interactions (i.e., $CO/Zn_{12}O_{12}$, $H_2S/Zn_{12}O_{12}$, $NH_3/Zn_{12}O_{12}$, $NO/Zn_{12}O_{12}$, and $NO_2/Zn_{12}O_{12}$) have relatively longer bonds. However, it was observed that at the tetragon positions of the $Zn_{12}O_{12}$ cluster, the gaseous molecules could be adsorbed on both the Zn and O atoms due to their respective high electropositive and electronegative nature. The highest bond length was observed between an atom of the Zn_{24} cluster and the O atom of CO (4.257 Å). Higher bond lengths were also observed in the CO_2/Zn_{24} and H_2S/Zn_{24} systems. The shortest bond length in this case is observed for the SO_2/Zn_{24} system, having lengths of 2.051 and 2.066 Å between two Zn atoms and two O atoms of the SO_2 gas molecule, as shown in Table 1.

3.2. HOMO−LUMO Analysis. The frontier molecular orbital (FMO) theory[76] has been employed to investigate the electrical conductivity and electronic stability of the compounds under study. The highest occupied molecular orbital (HOMO) and the lowest unoccupied molecular orbital (LUMO)[77] form the FMO. The results from the FMO analysis are provided in Table 2, including the HOMO and LUMO energy values, HOMO and LUMO energy gap (HLG), and descriptors such as chemical hardness (η), chemical potential (μ), and the electrophilicity index (ω). These parameters were calculated in order to assess the electronic stability of the systems under study. Figure 6 shows the HOMO−LUMO distribution and the associated energy gaps of $Zn_{12}O_{12}$ and Zn_{24} clusters at 0.01 isovalues, illustrating that before interaction with the gas molecules, the $Zn_{12}O_{12}$ and Zn_{24} clusters had energy gaps of 7.688 and 0.873 eV at the Fermi level of −4.085 and −3.594 eV, respectively.

Upon adsorption of CO onto the $Zn_{12}O_{12}$ and Zn_{24} clusters, the band gap increases slightly to 0.883 and 7.970 eV, respectively, compared to the pristine cases. Similar decreases in the band gap are also observed for the $NO_2/Zn_{12}O_{12}$ (7.414 eV), $NO/Zn_{12}O_{12}$ (7.215 eV), $SO_2/Zn_{12}O_{12}$ (6.892 eV), SO_2/Zn_{24} (0.471 eV), and NH_3/Zn_{24} (0.872 eV) systems. In

https://doi.org/10.1021/acsomega.3c01177
ACS Omega 2023, 8, 20621−20633

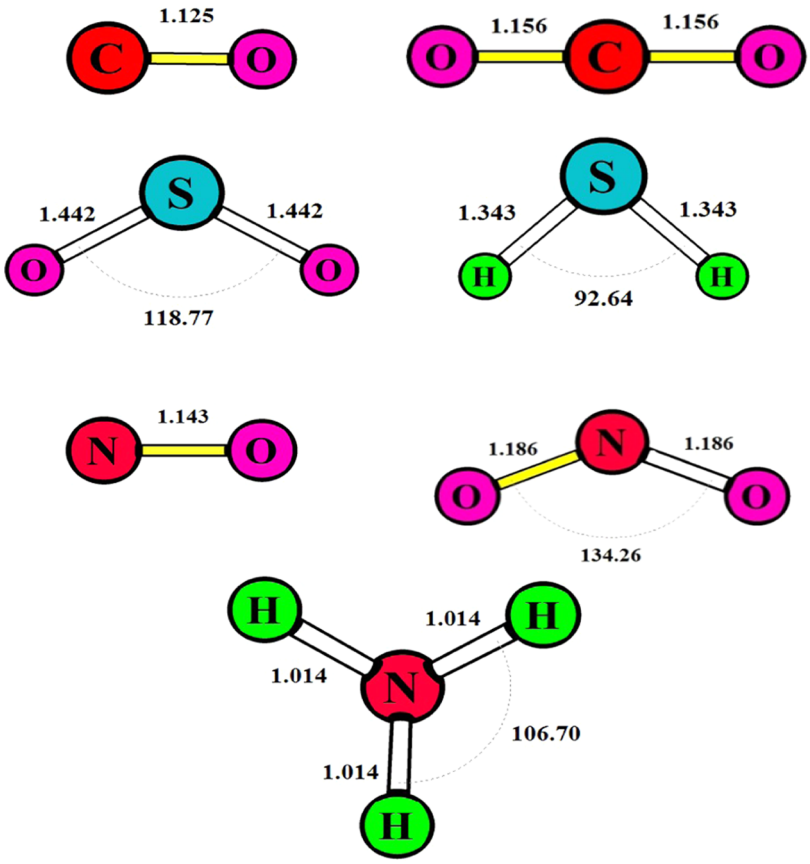

Figure 3. Interatomic distances (in Å) and angles (in rad) for CO, CO_2, H_2S, NH_3, NO, NO_2, and SO_2 determined by DFT calculations at the TPSSh/LANl2Dz computational level.

contrast, an increase in the band gap is observed upon the interaction of CO, CO_2, H_2S, and NH_3 with $Zn_{12}O_{12}$, having values of 7.967, 7.990, 7.890, and 7.999 eV, respectively. However, for the case of CO_2/Zn_{24}, H_2S/Zn_{24}, and NO_2/Zn_{24} system structures, the band gap is increased to 0.932, 0.961, and 0.921 eV, respectively. The electronic stability of the systems also increases when the energy gap increases, and vice versa. In turn, as the electronic stability increases, the electrical conductivity of the system decreases due to the increase in the energy gap. Considering that, we can deduce that the $CO/Zn_{12}O_{12}$, $CO_2/Zn_{12}O_{12}$, $NH_3/Zn_{12}O_{12}$, and $H_2S/Zn_{12}O_{12}$ systems are more stable than the pristine $Zn_{12}O_{12}$ cluster. Similarly, the CO/Zn_{24}, CO_2/Zn_{24}, and H_2S/Zn_{24} systems are also relatively stable. The CO/Zn_{24}, CO_2/Zn_{24}, NO_2/Zn_{24}, and H_2S/Zn_{24} systems have higher electronic stability compared to Zn_{24} due to their increased band gap, demonstrating stronger adsorption, whereas the NO/Zn_{24}, NH_3/Zn_{24}, and SO_2/Zn_{24}, systems all exhibit high conductivity due to their decreased band gap.

TDOS plots help to understand the distribution pattern of the HOMO and LUMO,[78] unveiling the molecular orbital composition and their contribution to chemical bonding visually when the discrete energy level is artificially curve broadened.[79] Density of state analysis has been performed in this study to further comprehend the orbital composition and contribution regarding the adsorption of the gases studied in this work. The TDOS plots for both isolated clusters are shown in Figure 7. Also, Figure 8 shows the TDOS plots of CO/Zn_{24} and $NO_2/Zn_{12}O_{12}$ systems as examples. The rest of the TDOS plots are provided in the SI (cf. Figures S1−S12).

The TDOS plots show that CO adsorbed on Zn_{24} has a large distribution of HOMO and LUMO orbital to the CO molecule and a narrow distribution of HOMO orbital to the Zn_{24} cluster but exhibits a wide distribution of LUMO orbital to Zn_{24}. These results suggest that charge density could be transferred from the HOMO of one species to the LUMO of the other species for the adsorption of CO onto the Zn_{24} cluster. For the adsorption of CO onto $Zn_{12}O_{12}$, there is an equal distribution of HOMO and LUMO charge density among the two species. A clear large band gap is observed in the TDOS plot of the $CO/Zn_{12}O_{12}$ system, which agrees with the energy difference between the HOMO and the LUMO obtained from the FMO analysis. On the other hand, the CO_2/Zn_{24} TDOS plot shows that charge density is distributed evenly across the HOMO and LUMO orbital, while in the case of the $CO_2/Zn_{12}O_{12}$ system, we observe a sharp peak at the HOMO, building confidence for the results reported in Table 2. Furthermore, in the $Zn_{12}O_{12}$ interaction with NO_2, the HOMO is only present in the NO_2 molecule, while the LUMO is distributed over the $Zn_{12}O_{12}$ cluster, suggesting a charge transfer from the NO_2 to the cluster may take place. Note that the interpretation of the TDOS plots for the CO/Zn_{24} and $NO_2/Zn_{12}O_{12}$ systems is rather elementary since the TDOS plots do not change considerably before and after adsorption.

DFT[80,81] can be used to qualitatively assess the electron affinity of the studied species through the electrophilicity index ($\omega = \mu^2/2\eta$) descriptor. Values of the chemical hardness (defined as $\eta = (IP - EA)/2$, where IP is ionization potential and EA the electron affinity) and chemical potential (estimated as $\mu = (\varepsilon_{LUMO} + \varepsilon_{HOMO})/2$) are listed in Table 2. According to

https://doi.org/10.1021/acsomega.3c01177
ACS Omega 2023, 8, 20621−20633

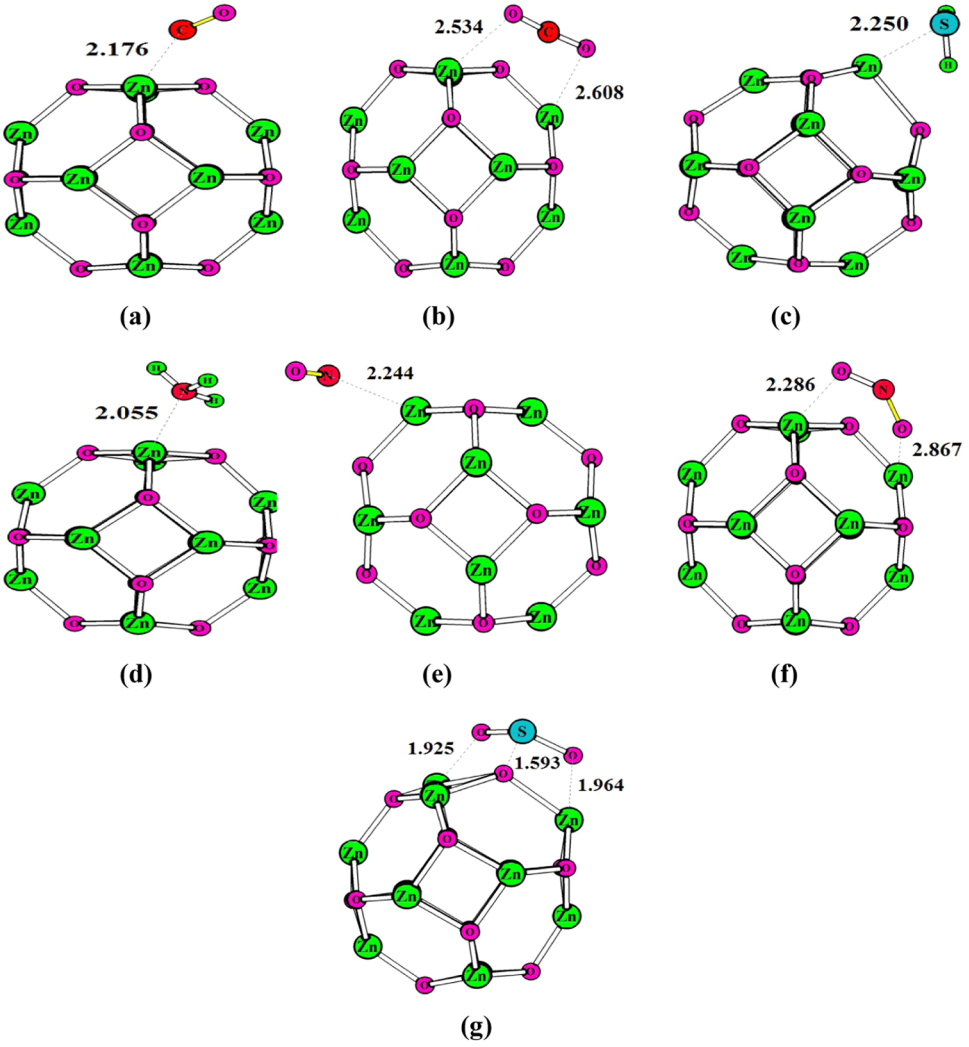

Figure 4. Optimized geometrical structure of (a) $CO/Zn_{12}O_{12}$, (b) $CO_2/Zn_{12}O_{12}$, (c) $H_2S/Zn_{12}O_{12}$, (d) $NH_3/Zn_{12}O_{12}$, (e) $NO/Zn_{12}O_{12}$, (f) $NO_2/Zn_{12}O_{12}$, and (g) $SO_2/Zn_{12}O_{12}$ systems obtained by DFT at the TPSSh/LANl2Dz level of theory. Interatomic distances are expressed in Å.

Koopmans'[82] and Janak's[83] approximations, the ionization potential is equal to the negative value of HOMO (i.e., $\varepsilon_{HOMO} = -IP$), and the electron affinity is equal to the negative value of LUMO (i.e., $\varepsilon_{LUMO} = -EA$). In this way, by having the numerical value of the electrophilicity index, one can predict the electron transfer from the donor to the acceptor species. The Zn_{24} cluster, with an electrophilicity value of 7.393, is the most effective species among all other systems studied in this work in terms of acting as an electron acceptor. Moreover, among the different gas species investigated in this work, SO_2 has an ω value of 2.28 (estimated in arbitrary units; au), indicating that it has a higher electron-accepting capability than any other gas species studied in this work and can accept electrons from the $Zn_{12}O_{12}$ cluster (ω = 1.09 au).

3.3. Adsorption Energies. The adsorption energies, E_{ads}, of all systems have been evaluated to determine the nature of adsorption (i.e., physisorption versus chemisorption) of the gases onto the $Zn_{12}O_{12}$ and Zn_{24} clusters. All E_{ads} values reported in Table 3 are negative, indicating favorable adsorptions in all cases. Based on these results, the strongest interaction is identified between SO_2 and the two clusters. Estimated E_{ads} values for SO_2, NH_3, NO_2, and NO, onto $Zn_{12}O_{12}$ are respectively −4.99, −1.03, −2.75, and −1.03 eV, suggesting chemisorption as a result of the transfer of charge between these two species (i.e., gas and cluster). In contrast, the $CO/Zn_{12}O_{12}$, $CO_2/Zn_{12}O_{12}$, and $H_2S/Zn_{12}O_{12}$ systems have low adsorption energy (i.e., −0.08, −0.11, and −0.13 eV, respectively), and can thus be characterized as physisorption. Similarly, the high adsorption energy of NO, NO_2, SO_2, and NH_3 onto Zn_{24} can be categorized as chemisorption, while the corresponding low E_{ads} of CO, CO_2, and H_2S as physisorption. Overall, the adsorption energy analysis suggests that $Zn_{12}O_{12}$ is a more effective adsorbent for SO_2, H_2S, NH_3, and CO_2, whereas Zn_{24} is for NO, NO_2, SO_2, and H_2S. These results are consistent with those obtained from the FMO analysis described above.

3.4. Natural Bond Orbital Analysis. The result of the Wiberg and Mayer bond order for both clusters are reported in Table 4. A reasonable amount of interactions exists between the $Zn_{12}O_{12}$ cluster and the investigated gases. Moreover, a strong interaction is observed between $Zn_{12}O_{12}$ and H_2S or SO_2 compared to the other gases. Furthermore, the adsorption of SO_2 onto Zn_{24} shows the strongest interaction among all cases. The corresponding WBI values for the pure $Zn_{12}O_{12}$ show similar results; i.e., strong interactions are observed between the surface of the cluster and the gases. The Zn_{24} cluster also exhibits stronger interaction with all of the gas molecules investigated here. Strong interactions are apparent

https://doi.org/10.1021/acsomega.3c01177
ACS Omega 2023, 8, 20621−20633

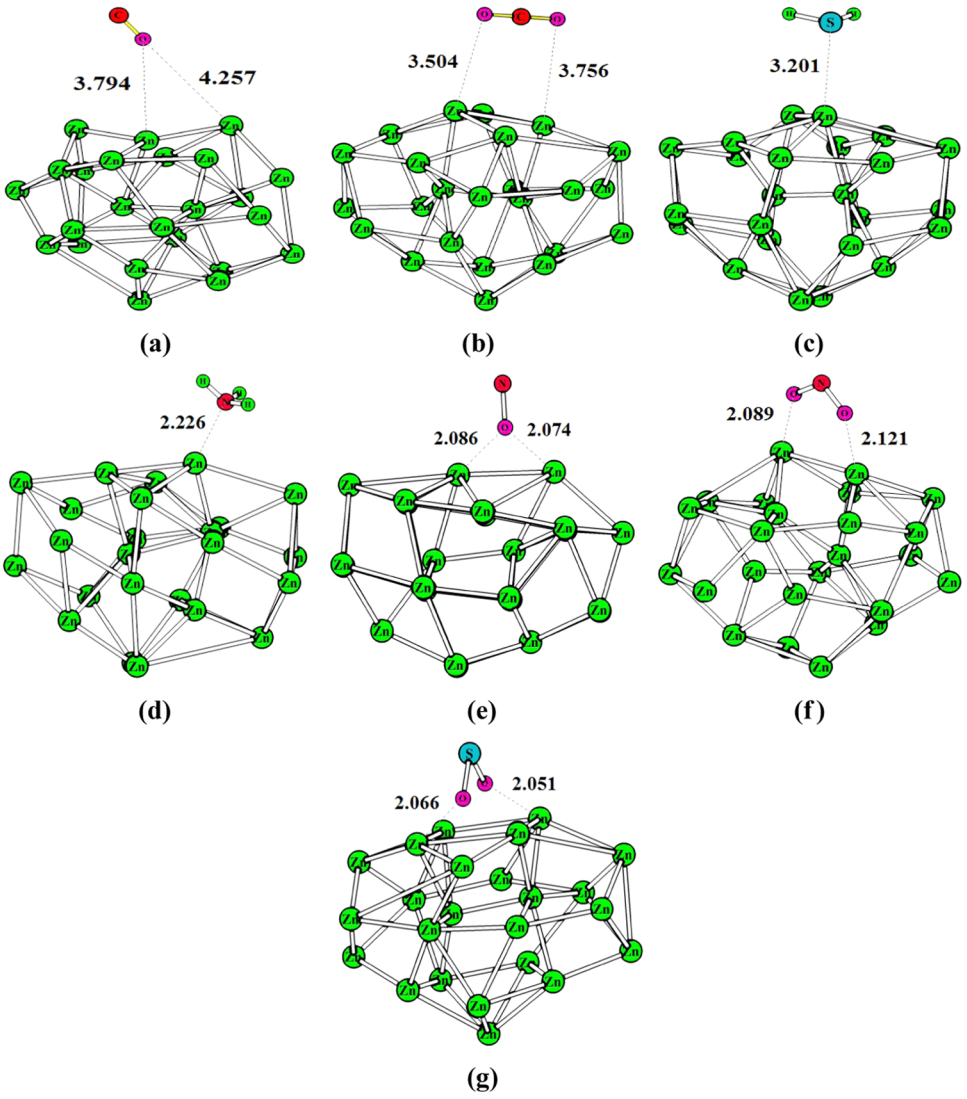

Figure 5. Optimized geometrical structure of (a) CO/Zn_{24}, (b) CO_2/Zn_{24}, (c) H_2S/Zn_{24}, (d) NH_3/Zn_{24}, (e) NO/Zn_{24}, (f) NO_2/Zn_{24}, and (g) SO_2/Zn_{24} systems obtained by DFT at the TPSSh/LANl2Dz level of theory. Interatomic distances are expressed in Å.

Table 1. Bond Lengths (in Å) for CO/Zn_{24}, CO_2/Zn_{24}, H_2S/Zn_{24}, NH_3/Zn_{24}, NO/Zn_{24}, NO_2/Zn_{24}, and SO_2/Zn_{24} and $CO/Zn_{12}O_{12}$, $CO_2/Zn_{12}O_{12}$, $H_2S/Zn_{12}O_{12}$, $NH_3/Zn_{12}O_{12}$, NO/Zn_{24}, $NO_2/Zn_{12}O_{12}$, and $SO_2/Zn_{12}O_{12}$ Systems Computed at the TPSSh/Lanl2Dz Level of Theory

system	interacting atoms	bond length	system	atoms	bond length
CO_2 Zn_{24}	Zn···O	3.504	CO_2-$Zn_{12}O_{12}$	Zn···O	2.534
	Zn···O	3.756		Zn···O	2.608
CO-Zn_{24}	Zn···O	3.794	CO-$Zn_{12}O_{12}$	Zn···C	2.176
H_2S-Zn_{24}	Zn···S	3.201	H_2S-$Zn_{12}O_{12}$	Zn···S	2.25
NH_3-Zn_{24}	Zn···N	2.226	NH_3-$Zn_{12}O_{12}$	Zn···N	2.055
NO_2-Zn_{24}	Zn···O	2.089	NO_2-$Zn_{12}O_{12}$	Zn···O	2.286
	Zn···O	2.121		Zn···O	2.867
NO-Zn_{24}	Zn···O	2.074	NO-$Zn_{12}O_{12}$	Zn···N	2.244
SO_2-Zn_{24}	Zn···O	2.051	SO_2-Zn12O_{12}	Zn···O	1.925
	Zn···O	2.066		Zn···O	1.964
				O···S	1.593

between the Zn_{24} cluster and NO, NO_2, or SO_2, with the former two gases comprising the strongest cases. According to the WBI values, as those reported in Table 4, Zn_{24} shows

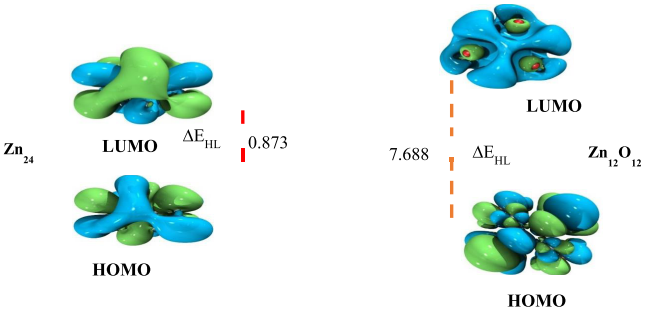

Figure 6. HOMO−LUMO distribution at 0.01 isovalue and energy gap (ΔE_{HL}) of $Zn_{12}O_{12}$ and Zn_{24} atomic clusters determined at the TPSSh/LANl2Dz level of theory.

stronger interaction with almost all of the gases when compared with $Zn_{12}O_{12}$, most likely due to greater charge transfer. The $Zn_{12}O_{12}$ cluster shows stronger interaction with H_2S when compared with Zn_{24}. Similar observations are also made for the cases of CO and CO_2. Both clusters show interactions of similar strength with SO_2. From these results, we can conclude that Zn_{24} can interact more strongly with NO,

https://doi.org/10.1021/acsomega.3c01177
ACS Omega 2023, 8, 20621−20633

Table 2. Conceptual DFT Parameters of Pristine Zn_{24} and $Zn_{12}O_{12}$ Clusters as well as for the CO, CO_2, H_2S, NH_3, NO, NO_2, and SO_2 Gas Molecules Together with Their Gas/Cluster Systems[a]

system	ε_{HOMO}	ε_{LUMO}	HLG	E_F	η	μ	ω
CO_2	−12.4998	1.2974	13.7973	−5.6012	6.8986	−5.6012	1.1369
CO	−12.6870	1.5886	14.2756	−5.5492	7.1378	−5.5492	1.0785
H_2S	−9.4350	2.3532	11.7882	−3.5409	5.8941	−3.5409	0.5318
NH_3	−9.3087	3.5190	12.8277	−2.8949	6.4139	−2.8949	0.3267
NO_2	−10.1177	−1.0479	9.0698	−5.5828	4.5349	−5.5828	1.7182
NO	−8.0875	0.4506	8.5381	−3.8184	4.2691	−3.8184	0.8538
SO_2	−11.3921	−1.8278	9.5643	−6.6099	4.7821	−6.6099	2.2841
Zn_{24}	−4.0306	−3.1571	0.8735	−3.5938	0.4367	−3.5938	7.3931
CO_2 Zn_{24}	−4.0398	−3.1070	0.9328	−3.5734	0.4664	−3.5734	6.8445
CO_Zn_{24}	−4.0156	−3.1331	0.8825	−3.5744	0.4412	−3.5744	7.2388
H_2S_Zn_{24}	−3.9516	−2.9905	0.9611	−3.4711	0.4806	−3.4711	6.2680
NH_3_Zn_{24}	−3.8915	−3.0199	0.8716	−3.4557	0.4358	−3.4557	6.8507
NO_2_Zn_{24}	−4.1315	−3.2109	0.9206	−3.6712	0.4603	−3.6712	7.3205
NO_Zn_{24}	−4.3348	−3.5386	0.7962	−3.9367	0.3981	−3.9367	9.7320
SO_2_Zn_{24}	−4.1933	−3.7222	0.4710	−3.9578	0.2355	−3.9578	16.6273
$Zn_{12}O_{12}$	−7.9283	−0.2408	7.6875	−4.0846	3.8437	−4.0846	1.0851
CO_2_$Zn_{12}O_{12}$	−7.9738	0.0166	7.9904	−3.9786	3.9952	−3.9786	0.9905
CO_$Zn_{12}O_{12}$	−7.8587	0.1113	7.9699	−3.8737	3.9850	−3.8737	0.9414
H_2S_$Zn_{12}O_{12}$	−7.8494	0.0403	7.8897	−3.9046	3.9448	−3.9046	0.9662
NH_3_$Zn_{12}O_{12}$	−7.6614	0.3374	7.9988	−3.6620	3.9994	−3.6620	0.8383
NO_2_$Zn_{12}O_{12}$	−7.9112	−0.4977	7.4135	−4.2044	3.7067	−4.2044	1.1922
NO_$Zn_{12}O_{12}$	−7.9221	−0.7075	7.2146	−4.3148	3.6073	−4.3148	1.2903
SO_2_Zn12O_{12}	−8.1425	−1.2501	6.8924	−4.6963	3.4462	−4.6963	1.6000

[a]Key: ε_{HOMO} is HOMO energy, ε_{LUMO} is LUMO energy, HLG indicates the HOMO−LUMO energy gap, E_F is the Fermi level, μ is the chemical potential, η is the chemical hardness, and ω is the electrophilicity index determined at TPSSh/LANl2Dz level of theory. All energy values are expressed in eV.

Table 3. Adsorption Energy (E_{ads}) of the Studied Systems Calculated at the TPSSh/LANl2Dz Level of Theory[a]

system ($Zn_{12}O_{12}$ cluster)	gas atom···cluster atom	E_{ads}	system (Zn_{24}cluster)	gas atom···cluster atom	E_{ads}
CO/$Zn_{12}O_{12}$	O···Zn	−0.54	CO/Zn_{24}	O···Zn	−0.08
CO/$Zn_{12}O_{12}$	C···Zn	−0.34	CO/Zn_{24}	C···Zn	−0.07
CO_2/$Zn_{12}O_{12}$	O···Zn	−0.58	CO_2/Zn_{24}	O···Zn	−0.11
H_2S/$Zn_{12}O_{12}$	S···Zn	−2.00	H_2S/Zn_{24}	S···Zn	−0.13
H_2S/$Zn_{12}O_{12}$	H···Zn	−0.98	H_2S/Zn_{24}	H···Zn	−0.04
NH_3/$Zn_{12}O_{12}$	N···Zn	−1.40	NH_3/Zn_{24}	N···Zn	−1.03
NH_3/$Zn_{12}O_{12}$	H···Zn	−0.66	NH_3/Zn_{24}	H···Zn	−0.87
NO/$Zn_{12}O_{12}$	N···Zn	−0.43	NO/Zn_{24}	N···Zn	−0.82
NO/$Zn_{12}O_{12}$	O···Zn	−0.36	NO/Zn_{24}	O···Zn	−1.03
NO_2/$Zn_{12}O_{12}$	N···Zn	−0.39	NO_2/Zn_{24}	N···Zn	−1.88
NO_2/$Zn_{12}O_{12}$	O···Zn	−0.55	NO_2/Zn_{24}	O···Zn	−2.75
SO_2/$Zn_{12}O_{12}$	S···Zn	−2.92	SO_2/Zn_{24}	S···Zn	−4.26
SO_2/$Zn_{12}O_{12}$	O···Zn	−2.64	SO_2/Zn_{24}	O···Zn	−4.99

[a]All values are expressed in eV.

NO_2, and SO_2 and therefore can act as a better adsorption agent for these gases than $Zn_{12}O_{12}$. In contrast, $Zn_{12}O_{12}$ can perform better as an adsorbent for H_2S, CO, and CO_2.

The natural electron configuration and partial natural charges are investigated using the NBO calculations provided in Tables S2 and S3 for gas/Zn_{24} and gas/$Zn_{12}O_{12}$ systems, respectively. The negative charges located on a typical atom have, in principle, higher electronegativity. The amount of charge transfer between the cluster and the gases can also be used as a reference to investigate the interaction between the cluster and the gases, such that the higher the charge transfers between the clusters and the gases, the stronger the interactions. The reported values in Tables S2 and S3 suggest that there is a significant charge transfer between the two species upon adsorption. For example, the amount of natural charge for oxygen atoms in the isolated SO_2 molecule is equal to −0.641, which is greatly increased to −1.153 after adsorption onto Zn_{24}. The corresponding natural electron configuration of the oxygen atom changes from [core]-2s(1.92)2p(4.72) to [core]2s(1.88)2p(5.26), indicating charge transfer to the 2p orbitals. In the same way, the charge transfer process between the gases and the aforementioned clusters can be recognized (cf. data provided in Tables S2 and S3).

3.5. Noncovalent Interaction and Quantum Theory of Atom in Molecule Analysis. The RDG (y-axis) and the scatter graph of the sign $\lambda_2(\mathbf{r})\rho(\mathbf{r})$ product (x-axis) are provided in the supplement (cf. Figures S13−S26). The nature of interacting forces, such as the electrostatic/strong non-

https://doi.org/10.1021/acsomega.3c01177
ACS Omega 2023, 8, 20621−20633

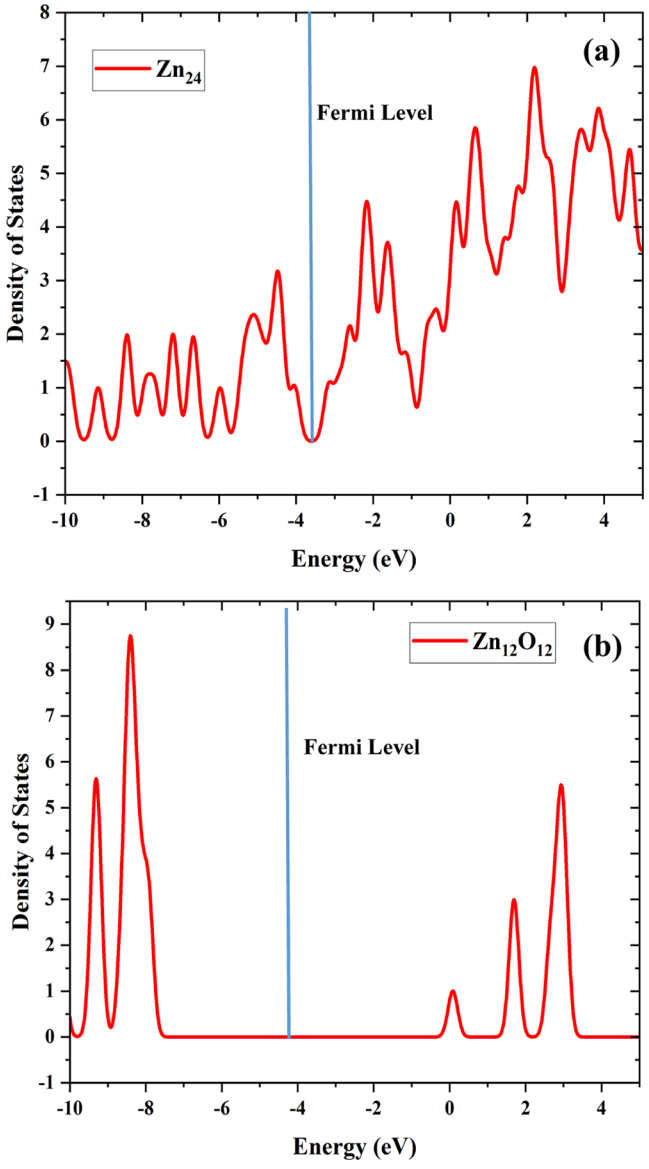

Figure 7. TDOS plots for the isolated (a) Zn_{24} and (b) $Zn_{12}O_{12}$ clusters calculated at the TPSSh/LANl2Dz level of theory.

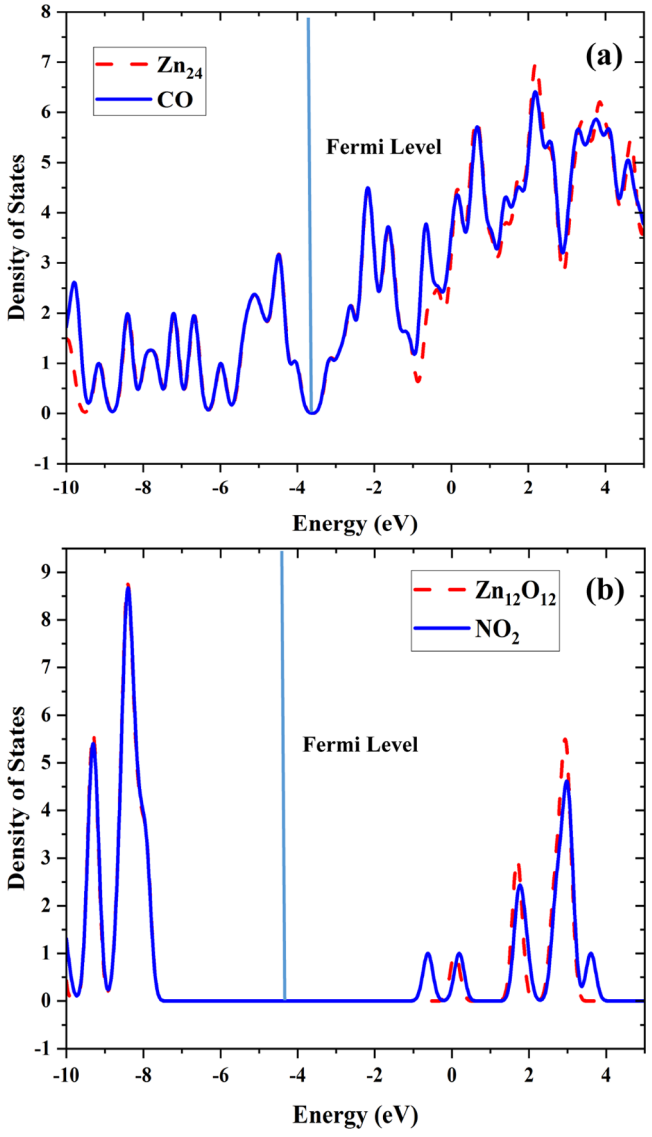

Figure 8. TDOS plots for (a) CO/Zn_{24} and (b) $NO_2/Zn_{12}O_{12}$ systems calculated at the TPSSh/LANl2Dz level of theory.

covalent force (hydrogen bonding), dispersion/weak noncovalent force, and steric repulsion, are differentiated by blue, green, and red colors, respectively, in Figures S13–S26.[84] From these figures, we can see that the interactions between the gases and the Zn_{24} cluster are both electrostatic noncovalent and dispersion noncovalent. From the RDG isosurface, we can confirm that a strong noncovalent force of attraction is an intramolecular interaction. In the $Zn_{12}O_{12}$ interaction with the gases, the red spots in the NCI figures are observed on the surfaces; in other words, a steric repulsion exists within the surface. As evident from the RDG iso-surface, there is an inter- and intramolecular steric effect, indicating a repulsive force felt in $Zn_{12}O_{12}$ interaction with NO_2. However, a strong intramolecular force of attraction between $Zn_{12}O_{12}$ and NO, NH_3, and H_2S gases can also be observed.

The results from the QTAIM analysis carried out in the paper are reported in Table 5. From these results, we can conclude that on the adsorption site, the Laplacian of electron density energy is positive, implying that the bonds are noncovalent. This result is corroborated by the high G/|V| ratios. We find that this ratio has a value that is greater than 0.5 and very close to 1; consequently, it can be classified as noncovalent. For a better understanding of the location of critical points and interaction paths, the readers are referred to Figures S27–S40 in the SI.

Table 4. Mayer and Wiberg Bond Index (WBI) Estimated for Intramolecular Interactions between the Clusters and the Gases Determined at the TPSSh/LANl2Dz Level of Theory

$Zn_{12}O_{12}$ cluster			Zn_{24} cluster		
systems	Mayer	Wiberg	systems	Mayer	Wiberg
$CO/Zn_{12}O_{12}$	0.315	0.539	CO/Zn_{24}	0.125	0.128
$CO_2/Zn_{12}O_{12}$	0.293	0.405	CO_2/Zn_{24}	0.165	0.151
$H_2S/Zn_{12}O_{12}$	1.363	1.917	H_2S/Zn_{24}	0.103	0.372
$NH_3/Zn_{12}O_{12}$	0.423	0.578	NH_3/Zn_{24}	0.364	0.579
$NO/Zn_{12}O_{12}$	0.334	0.481	NO/Zn_{24}	2.82	4.45
$NO_2/Zn_{12}O_{12}$	0.253	0.341	NO_2/Zn_{24}	1.03	1.409
$SO_2/Zn_{12}O_{12}$	1.789	2.488	SO_2/Zn_{24}	1.84	2.86

https://doi.org/10.1021/acsomega.3c01177
ACS Omega 2023, 8, 20621−20633

Table 5. QTAIM Topology Parameters, Including Electron Density $\rho(r)$, Laplacian of Electron Density $\nabla^2\rho(r)$, Kinetic Electron Density $G(r)$, Potential of Electron Density $V(r)$, and $G(r)/V(r)$ Ratio of the Gases on Zn_{24} and $Zn_{12}O_{12}$ at theTPSSh/LANl2Dz Level of Theory

systems	bond	$\rho(r)$	$\nabla^2\rho(r)$	$G(r)$	$V(r)$	$G/\|V\|$
$CO/Zn_{12}O_{12}$	C···Zn	0.0568	0.1698	0.0559	−0.0694	0.8059
$CO_2/Zn_{12}O_{12}$	C···O	0.0252	0.0765	0.0201	−0.021	0.9548
	O···Zn	0.0196	0.0872	0.0209	−0.0201	1.0423
$H_2S/Zn_{12}O_{12}$	S···Zn	0.0785	0.16	0.064	−0.0881	0.727
$NH_3/Zn_{12}O_{12}$	N···Zn	0.0742	0.3079	0.0924	−0.1079	0.8567
	H···O	0.0309	0.1139	0.0278	−0.0272	1.0233
$NO/Zn_{12}O_{12}$	N···Zn	0.0438	0.1647	0.0477	−0.0543	0.879
	N···O	0.0313	0.1088	0.0256	−0.0241	1.0653
$NO_2/Zn_{12}O_{12}$	O···Zn	0.0368	0.1506	0.0412	−0.0448	0.9203
	O···O	0.0114	0.0369	0.0088	−0.0083	1.057
$SO_2/Zn_{12}O_{12}$	S···O	0.2268	0.0611	0.2877	−0.5602	0.5136
	O···Zn	0.0833	0.4275	0.1178	−0.1288	0.915
CO/Zn_{24}					−	
CO_2/Zn_{24}	C···Zn	0.307	0.666	0.133	−0.1	1.33
H_2S/Zn_{24}	S···Zn	0.134	0.254	0.657	−0.696	0.944
NH_3/Zn_{24}	N···Zn	0.473	0.197	0.48	−0.574	0.836
NO/Zn_{24}	O···Zn	0.549	0.298	0.659	−0.727	0.906
	O···Zn	0.558	0.31	0.684	−0.752	0.754
NO_2/Zn_{24}	O···Zn	0.535	0.292	0.64	−0.701	0.912
	O···Zn	0.492	0.255	0.573	−0.633	0.905
SO_2/Zn_{24}	O···Zn	0.583	0.326	0.717	−0.79	0.906
	O···Zn	0.622	0.366	0.791	−0.865	0.914
	O···Zn	0.589	0.331	0.728	−0.801	0.909
	O···Zn	0.6	0.346	0.754	−0.826	0.913

4. CONCLUSIONS

We have employed DFT with the TPSSh functional and the LANl2Dz basis set to study the adsorption of CO, CO_2, H_2S, NH_3, NO, NO_2, and SO_2 onto $Zn_{12}O_{12}$ and Zn_{24} clusters. We found that the band gap of the Zn_{24} clusters decreases marginally upon adsorption of NH_3, NO, and SO_2, whereas it increases upon adsorption of CO, CO_2, H_2S, and NO_2, indicating an increase in the stability of the resulting system. Similarly, $Zn_{12}O_{12}$ exhibits a decrease in the energy gap upon adsorption of NO, NO_2, and SO_2 and an increase for CO, CO_2, H_2S, and NH_3. Both clusters exhibit favorable adsorption toward all of the gas species since all of the calculated adsorption energies are negative. The highest energy was observed for the adsorption of SO_2 on both Zn_{24} (− 4.99 eV) and $Zn_{12}O_{12}$ (− 2.92 eV) clusters. The lowest adsorption energies among the studied systems were observed for the adsorption of CO on Zn_{24} (−0.08 eV) and of NO on $Zn_{12}O_{12}$ (−0.43 eV). The adsorption of NO and NO_2 is favored on the Zn_{24} than the $Zn_{12}O_{12}$ cluster. In contrast, the adsorption of CO, CO_2, H_2S, and NH_3 on $Zn_{12}O_{12}$ releases more energy than on the Zn_{24} cluster. NBO analysis shows that there is a strong intermolecular interaction between the gases and clusters. The strongest intermolecular interaction was identified for the SO_2/Zn_{24} system, in accordance with the high adsorption energy observed for this system. Similarly, the $SO_2/Zn_{12}O_{12}$ interaction was observed to be the strongest among all gases studied for $Zn_{12}O_{12}$. Stronger intermolecular interaction has also been observed for the adsorption of NO, NO_2, and SO_2 onto Zn_{24} than $Zn_{12}O_{12}$, whereas the opposite is predicted for the adsorption of CO, CO_2, H_2S, and NH_3. These intermolecular interactions are identified as noncovalent by the NCI analysis. QTAIM analysis also shows that closed-shell interactions prevail for NO, NO_2, and SO_2 with both atomic clusters. In summary, both clusters can act as good adsorbent materials for the gases investigated here, with Zn_{24} exhibiting a higher preference for SO_2, NO, and NO_2, whereas $Zn_{12}O_{12}$ for CO, CO_2, and H_2S.

■ ASSOCIATED CONTENT

Supporting Information

The Supporting Information is available free of charge at https://pubs.acs.org/doi/10.1021/acsomega.3c01177.

Additional information on the quantum chemical analyses, including TDOS; NBO; NCI; and QTAIM (PDF)

■ AUTHOR INFORMATION

Corresponding Authors

Mohsen Doust Mohammadi − *Climate and Atmosphere Research Centre, The Cyprus Institute, Nicosia 2121, Cyprus;* orcid.org/0000-0003-2449-2962; Email: m.d.mohammadi@cyi.ac.cy

George Biskos − *Climate and Atmosphere Research Centre, The Cyprus Institute, Nicosia 2121, Cyprus; Faculty of Civil Engineering and Geosciences, Delft University of Technology, Delft 2628CN, The Netherlands*; Email: g.biskos@cyi.ac.cy

Authors

Hitler Louis − *Computational and Bio-Simulation Research Group, University of Calabar, Calabar 540221, Nigeria*

Udochukwu G. Chukwu − *Computational and Bio-Simulation Research Group, University of Calabar, Calabar 540221, Nigeria;* orcid.org/0000-0001-6934-394X

Somnath Bhowmick − *Climate and Atmosphere Research Centre, The Cyprus Institute, Nicosia 2121, Cyprus;* orcid.org/0000-0001-7498-2463

https://doi.org/10.1021/acsomega.3c01177
ACS Omega 2023, 8, 20621−20633

Michael E. Rasaki − *Computational and Bio-Simulation Research Group, University of Calabar, Calabar 540221, Nigeria*

Complete contact information is available at: https://pubs.acs.org/10.1021/acsomega.3c01177

Notes

The authors declare no competing financial interest.

■ ACKNOWLEDGMENTS

M.D.M., S.B., and G.B. acknowledge the financial support of the European Regional Development Fund and the Republic of Cyprus through the Research Promotion Foundation NANO²LAB Project INFRASTRUCTURES/1216/0070. This research was also supported by the EMME-CARE project that has received funding from the European Union's Horizon 2020 Research and Innovation Program, under Grant Agreement No. 856612, as well as matching cofunding by the Government of the Republic of Cyprus. The authors thank the AMD EPYC High Performance Computing Facility of The Cyprus Institute for computational resources.

■ REFERENCES

(1) Zhao, Y.; Hu, J.; Tan, Z.; Liu, T.; Zeng, W.; Li, X.; Huang, C.; Wang, S.; Huang, Z.; Ma, W. Ambient carbon monoxide and increased risk of daily hospital outpatient visits for respiratory diseases in Dongguan, China. *Sci. Total Environ.* **2019**, *668*, 254−260.

(2) Lambert, T. W.; Goodwin, V. M.; Stefani, D.; Strosher, L. Hydrogen sulfide (H2S) and sour gas effects on the eye. A historical perspective. *Sci. Total Environ.* **2006**, *367*, 1−22.

(3) Asghar, U.; Rafiq, S.; Anwar, A.; Iqbal, T.; Ahmed, A.; Jamil, F.; Khurram, M. S.; Akbar, M. M.; Farooq, A.; Shah, N. S.; Park, Y. K. Review on the progress in emission control technologies for the abatement of CO2, SOx and NOx from fuel combustion. *J. Environ. Chem. Eng.* **2021**, *9*, No. 106064.

(4) Aigbedion, I.; Iyayi, S. E. Environmental effect of mineral exploitation in Nigeria. *Int. J. Phys. Sci.* **2007**, *2*, 33−38.

(5) Häberle, J.; Chakrapani, A.; Ah Mew, N.; Longo, N. Hyperammonaemia in classic organic acidaemias: a review of the literature and two case histories. *Orphanet J. Rare Dis.* **2018**, *13*, No. 219.

(6) Pandey, J. S.; Kumar, R.; Devotta, S. Health risks of NO2, SPM and SO2 in Delhi (India). *Atmospheric Environment* **2005**, *39*, 6868−6874.

(7) Yoro, K. O.; Daramola, M. O. CO2 emission sources, greenhouse gases, and the global warming effect. In *Advances in Carbon Capture*; Elsevier, 2020; pp 3−28.

(8) Nurhisanah, S.; Hasyim, H. Environmental health risk assessment of sulfur dioxide (SO2) at workers around in combined cycle power plant (CCPP). *Heliyon* **2022**, *8*, No. e09388.

(9) Stetter, J. R.; Li, J. Amperometric gas sensors a review. *Chem. Rev.* **2008**, *108*, 352−366.

(10) Kumar, P.; Morawska, L.; Martani, C.; Biskos, G.; Neophytou, M.; Di Sabatino, S.; Bell, M.; Norford, L.; Britter, R. The rise of low-cost sensing for managing air pollution in cities. *Environ. Int.* **2015**, *75*, 199−205.

(11) Isaac, N. A.; Pikaar, I.; Biskos, G. Metal oxide semiconducting nanomaterials for air quality gas sensors: operating principles, performance, and synthesis techniques. *Microchim. Acta* **2022**, *189*, 196.

(12) Cross, E. S.; Williams, L. R.; Lewis, D. K.; Magoon, G. R.; Onasch, T. B.; Kaminsky, M. L.; Worsnop, D. R.; Jayne, J. T. Use of electrochemical sensors for measurement of air pollution: correcting interference response and validating measurements. *Atmos. Meas.Tech.* **2017**, *10*, 3575−3588.

(13) Isaac, N. A.; Pikaar, I.; Biskos, G. Metal oxide semiconducting nanomaterials for air quality gas sensors: operating principles, performance, and synthesis techniques. *Microchim. Acta* **2022**, *189*, 1−22.

(14) Buckley, D. J.; Black, N. C.; Castanon, E. G.; Melios, C.; Hardman, M.; Kazakova, O. Frontiers of graphene and 2D material-based gas sensors for environmental monitoring. *2D Mater.* **2020**, *7*, No. 032002.

(15) Imran, M.; Motta, N.; Shafiei, M. Electrospun one-dimensional nanostructures: a new horizon for gas sensing materials. *Beilstein J. Nanotechnol.* **2018**, *9*, 2128−2170.

(16) Yari, S.; Mahdavian, L.; Dehghanpour, N. Computational Investigation for the Removal of Hydrocarbon Sulfur Compounds by Zinc Oxide Nano-Cage (Zn12O12-NC). *Polycycl. Aromat. Compd.* **2023**, *43*, 370−383.

(17) Baei, M. T. DFT Study of CO 2 adsorption on the Zn 12 O 12 nano-cage. *Bull. Korean Chem. Soc.* **2013**, *34*, 3722−3726.

(18) Peyghan, A. A.; Baei, M. T.; Hashemian, S. ZnO nanocluster as a potential catalyst for dissociation of H 2 S molecule. *J. Cluster Sci.* **2013**, *24*, 341−347.

(19) Beheshtian, J.; Peyghan, A. A.; Bagheri, Z. Adsorption and dissociation of Cl2 molecule on ZnO nanocluster. *Appl. Surf. Sci.* **2012**, *258*, 8171−8176.

(20) Weintraub, B.; Zhou, Z.; Li, Y.; Deng, Y. Solution synthesis of one-dimensional ZnO nanomaterials and their applications. *Nanoscale* **2010**, *2*, 1573−1587.

(21) Doust Mohammadi, M.; Abbas, F.; Louis, H.; Mathias, G. E.; Unimuke, T. O. Trapping of CO, CO2, H2S, NH3, NO, NO2, and SO2 by Polyoxometalate compound. *Comput. Theor. Chem.* **2022**, *1215*, No. 113826.

(22) Doust Mohammadi, M.; Abdullah, H. Y.; Kalamse, V. G.; Chaudhari, A. Interaction of halomethane CH3Z (Z = F, Cl, Br) with X12Y12 (X = B, Al, Ga & Y = N, P, As) nanocages. *Comput. Theor. Chem.* **2022**, *1208*, No. 113544.

(23) Rahman, M. M.; Alam, M.; Asiri, A. M. Potential application of mixed metal oxide nanoparticle-embedded glassy carbon electrode as a selective 1, 4-dioxane chemical sensor probe by an electrochemical approach. *RSC Adv.* **2019**, *9*, 42050−42061.

(24) Kartika, R.; Alsultany, F. H.; Jalil, A. T.; Mahmoud, M. Z.; Fenjan, M. N.; Rajabzadeh, H. Ca12O12 nanocluster as highly sensitive material for the detection of hazardous mustard gas: Density-functional theory. *Inorg. Chem. Commun.* **2022**, *137*, No. 109174.

(25) Liu, M.-H.; Chen, Y.-W.; Lin, T.-S.; Mou, C.-Y. Defective mesocrystal ZnO-supported gold catalysts: facilitating CO oxidation via vacancy defects in ZnO. *ACS Catal.* **2018**, *8*, 6862−6869.

(26) Esrafili, M. D.; Arjomandi Rad, F. CO oxidation mediated by Al-doped ZnO nanoclusters: A first-principles investigation. *Int. J. Quantum Chem.* **2022**, *122*, No. e26873.

(27) Yong, Y.; Su, X.; Zhou, Q.; Kuang, Y.; Li, X. The Zn12O12 cluster-assembled nanowires as a highly sensitive and selective gas sensor for NO and NO2. *Sci. Rep.* **2017**, *7*, No. 17505.

(28) Afshari, T.; Mohsennia, M. Transition metals doped ZnO nanocluster for ethylene oxide detection: A DFT study. *Main Group Met. Chem.* **2019**, *42*, 113−120.

(29) Salmankhani, A.; Karami, Z.; Mashhadzadeh, A. H.; Ganjali, M. R.; Vatanpour, V.; Esmaeili, A.; Habibzadeh, S.; Saeb, M. R.; Fierro, V.; Celzard, A. New insights into H2S adsorption on graphene and graphene-like structures: a comparative DFT study. *C* **2020**, *6*, No. 74.

(30) Louis, H.; Patrick, M.; Amodu, I. O.; Benjamin, I.; Ikot, I. J.; Iniama, G. E.; Adeyinka, A. S. Sensor behavior of transition-metals (X = Ag, Au, Pd, and Pt) doped Zn11-X-O12 nanostructured materials for the detection of serotonin. *Mater. Today Commun.* **2023**, *34*, No. 105048.

(31) Mukhlif, B. A.; Patra, I.; Kumar, T. C. A.; Sivaraman, R.; Saadoon, N.; Obaid, N. H.; Kumar, N. B.; Mustafa, Y. F. Investigate the effect of Zn12O12, AlZn11O12, and GaZn11O12 nanoclusters in the carbamazepine drug detection in gas and solvent phases: a

comparative DFT study. *Monatsh. Chem.-Chem. Mon.* **2023**, *154*, 171−179.
(32) Muz, İ.; Kurban, M. Zinc oxide nanoclusters and their potential application as CH4 and CO2 gas sensors: Insight from DFT and TD-DFT. *J. Comput. Chem.* **2022**, *43*, 1839−1847.
(33) Wang, J.; Wang, G.; Zhao, J. Nonmetal-metal transition in Zn n (n = 2−2 0) clusters. *Phys. Rev. A* **2003**, *68*, No. 013201.
(34) Kiely, E.; Zwane, R.; Fox, R.; Reilly, A. M.; Guerin, S. Density functional theory predictions of the mechanical properties of crystalline materials. *CrystEngComm* **2021**, *23*, 5697−5710.
(35) Peng, B.; Van Kuiken, B. E.; Ding, F.; Li, X. A guided self-consistent-field method for excited-state wave function optimization: Applications to ligand-field transitions in transition-metal complexes. *J. Chem. Theory Comput.* **2013**, *9*, 3933−3938.
(36) Vuckovic, S. Quantification of geometric errors made simple: application to main-group molecular structures. *J. Phys. Chem. A* **2022**, *126*, 1300−1311.
(37) Staroverov, V. N.; Scuseria, G. E.; Tao, J.; Perdew, J. P. Comparative assessment of a new nonempirical density functional: Molecules and hydrogen-bonded complexes. *J. Chem. Phys.* **2003**, *119*, 12129−12137.
(38) Barone, V.; Hod, O.; Peralta, J. E.; Scuseria, G. E. Accurate prediction of the electronic properties of low-dimensional graphene derivatives using a screened hybrid density functional. *Acc. Chem. Res.* **2011**, *44*, 269−279.
(39) Jacquemin, D.; Wathelet, V.; Perpete, E. A.; Adamo, C. Extensive TD-DFT benchmark: singlet-excited states of organic molecules. *J. Chem. Theory Comput.* **2009**, *5*, 2420−2435.
(40) Roosevelt, T., Benchmarks for HS-LS energy difference: NEVPT2, CASPT2 and DLPNO-CCSD (T) vs. TPSSh. *Theoretical study of the excited state lifetime by ligand modifications and the vibrational anharmonicity for Fe (II) and Ru (II) complexes*, 91.
(41) Sajjad, S.; Maria; Mahmood, T.; Ayub, K. Benchmark study of structural and vibrational properties of scandium clusters. *J. Mol. Struct.* **2017**, *1142*, 139−147.
(42) Azpiroz, J. M.; Ugalde, J. M.; Infante, I. Benchmark assessment of density functional methods on group II−VI MX (M = Zn, Cd; X = S, Se, Te) quantum dots. *J. Chem. Theory Comput.* **2014**, *10*, 76−89.
(43) Olejniczak, A.; Cichy, B.; Stręk, W. DFT calculations of metal-organic I-III-VI semiconductor clusters: Benchmark of exchange-correlation functionals and localized basis sets. *Comput. Mater. Sci.* **2019**, *163*, 186−195.
(44) Frisch, M. J.; Trucks, G. W.; Schlegel, H. B.; Scuseria, G. E.; Robb, M. A.; Cheeseman, J. R.; Scalmani, G.; Barone, V.; Petersson, G. A.; Nakatsuji, H.; Li, X.; Caricato, M.; Marenich, A. V.; Bloino, J.; Janesko, B. G.; Gomperts, R.; Mennucci, B.; Hratchian, H. P.; Ortiz, J. V.; Izmaylov, A. F.; Sonnenberg, J. L.; Williams-Young, D.; Ding, F.; Lipparini, F.; Egidi, F.; Goings, J.; Peng, B.; Petrone, A.; Henderson, T.; Ranasinghe, D.; Zakrzewski, V. G.; Gao, J.; Rega, N.; Zheng, G.; Liang, W.; Hada, M.; Ehara, M.; Toyota, K.; Fukuda, R.; Hasegawa, J.; Ishida, M.; Nakajima, T.; Honda, Y.; Kitao, O.; Nakai, H.; Vreven, T.; Throssell, K.; Montgomery, J. A., Jr.; Peralta, J. E.; Ogliaro, F.; Bearpark, M. J.; Heyd, J. J.; Brothers, E. N.; Kudin, K. N.; Staroverov, V. N.; Keith, T. A.; Kobayashi, R.; Normand, J.; Raghavachari, K.; Rendell, A. P.; Burant, J. C.; Iyengar, S. S.; Tomasi, J.; Cossi, M.; Millam, J. M.; Klene, M.; Adamo, C.; Cammi, R.; Ochterski, J. W.; Martin, R. L.; Morokuma, K.; Farkas, O.; Foresman, J. B.; Fox, D. J. *Gaussian 16*; Revision C.01; Gaussian, Inc.: Wallingford CT, 2016.
(45) O'boyle, N. M.; Tenderholt, A. L.; Langner, K. M. Cclib: a library for package-independent computational chemistry algorithms. *J. Comput. Chem.* **2008**, *29*, 839−845.
(46) Lu, T.; Chen, F. Multiwfn: A multifunctional wavefunction analyzer. *J. Comput. Chem.* **2012**, *33*, 580−592.
(47) Humphrey, W.; Dalke, A.; Schulten, K. VMD: visual molecular dynamics. *J. Mol. Graphics* **1996**, *14*, 33−38.
(48) Zhurko, G. A.; Zhurko, D. A. *ChemCraft 1.6*, 2008.
(49) Agwupuye, J. A.; Louis, H.; Unimuke, T. O.; David, P.; Ubana, E. I.; Moshood, Y. L. Electronic structure investigation of the stability, reactivity, NBO analysis, thermodynamics, and the nature of the interactions in methyl-substituted imidazolium-based ionic liquids. *J. Mol. Liq.* **2021**, *337*, No. 116458.
(50) Doust Mohammadi, M.; Abdullah, H. Y. Adsorption of 1-chloro-1, 2, 2, 2-tetrafluoroethane on pristine, Al, Ga-doped boron nitride nanotubes: a study involving PBC-DFT, NBO analysis, and QTAIM. *Can. J. Chem.* **2021**, *99*, 51−62.
(51) Tarika, J. D.; Dexlin, X. D.; Arun kumar, A.; Rathika, A.; Jayanthi, D. D.; Beaula, T. J. Computational Insights On Charge Transfer and Non-covalent Interactions of Antibacterial Compound 4-dimethylaminopyridinium pyridine-2-carboxylate pentahydrate. *J. Mol. Struct.* **2022**, *1256*, No. 132525.
(52) Doust Mohammadi, M.; Abdullah, H. Y. The adsorption of bromochlorodifluoromethane on pristine and Ge-doped silicon carbide nanotube: a PBC-DFT, NBO, and QTAIM study. *Struct. Chem.* **2021**, *32*, 481−494.
(53) Doust Mohammadi, M.; Salih, I. H.; Abdullah, H. Y. The adsorption of chlorofluoromethane on pristine and Ge-doped silicon carbide nanotube: a PBC-DFT, NBO, and QTAIM study. *Mol. Simul.* **2020**, *46*, 1405−1416.
(54) Eno, E. A.; Louis, H.; Unimuke, T. O.; Gber, T. E.; Mbonu, I. J.; Ndubisi, C. J.; Adalikwu, S. A. Reactivity, stability, and thermodynamics of para-methylpyridinium-based ionic liquids: Insight from DFT, NCI, and QTAIM. *J. Ionic Liq.* **2022**, *2*, No. 100030.
(55) Damej, M.; Kaya, S.; Ibrahimi, B. E.; Lee, H.; Molhi, A.; Serdaroğlu, G.; Benmessaoud, M.; Ali, I.; Hajjaji, S. E.; Lgaz, H. The corrosion inhibition and adsorption behavior of mercaptobenzimidazole and bis-mercaptobenzimidazole on carbon steel in 1.0 M HCl: Experimental and computational insights. *Surf. Interfaces* **2021**, *24*, No. 101095.
(56) Bridgeman, A. J.; Cavigliasso, G.; Ireland, L. R.; Rothery, J. The Mayer bond order as a tool in inorganic chemistry. *J. Chem. Soc., Dalton Trans.* **2001**, *14*, 2095−2108.
(57) Müller, P. C.; Ertural, C.; Hempelmann, J.; Dronskowski, R. Crystal orbital bond index: covalent bond orders in solids. *J. Phys. Chem. C* **2021**, *125*, 7959−7970.
(58) Doust Mohammadi, M.; Hamzehloo, M. The adsorption of bromomethane onto the exterior surface of aluminum nitride, boron nitride, carbon, and silicon carbide nanotubes: a PBC-DFT, NBO, and QTAIM study. *Comput.Theoret. Chem.* **2018**, *1144*, 26−37.
(59) Zhang, J. X.; Sheong, F. K.; Lin, Z. Unravelling chemical interactions with principal interacting orbital analysis. *Chem. − Eur. J.* **2018**, *24*, 9639−9650.
(60) Ravaei, I.; Azami, S. M. Block deformation analysis: Density matrix blocks as intramolecular deformation density. *J. Comput. Chem.* **2020**, *41*, 2446−2458.
(61) Otero-De-La-Roza, A.; Johnson, E. R.; Contreras-García, J. Revealing non-covalent interactions in solids: NCI plots revisited. *Phys. Chem. Chem. Phys.* **2012**, *14*, 12165−12172.
(62) Sheeba, B. Q.; Michael Mary, M. S.; Amalanathan, M.; Job, C. B. Structural and vibrational spectral investigation on the identification of Non-Linear Optical properties and wave function analyses (electrostatic potential, electron localisation function, localised orbital locator) of 3-Ethoxy Salicilaldehyde. *Mol. Simul.* **2021**, *47*, 1217−1233.
(63) Cortés-Arriagada, D. Elucidating the co-transport of bisphenol A with polyethylene terephthalate (PET) nanoplastics: A theoretical study of the adsorption mechanism. *Environment. Pollut.* **2021**, *270*, No. 116192.
(64) Wang, L.; Liu, Y.-L.; He, D.; Chen, S.-H.; Li, Q.-J.; Wang, M.-S. The nonlinear optical properties and noncovalent interactions of supramolecular Donor− acceptor− donor assemblies between molecular tweezers and fullerenes. *J. Lumin.* **2022**, *250*, No. 119094.
(65) Cukrowski, I.; de Lange, J. H.; Adeyinka, A. S.; Mangondo, P. Evaluating common QTAIM and NCI interpretations of the electron density concentration through IQA interaction energies and 1D cross-sections of the electron and deformation density distributions. *Comput.Theoret. Chem.* **2015**, *1053*, 60−76.

https://doi.org/10.1021/acsomega.3c01177
ACS Omega 2023, 8, 20621−20633

(66) Bader, R. F. W.; Anderson, S.; Duke, A. Quantum topology of molecular charge distributions. 1. *J. Am. Chem. Soc.* **1979**, *101*, 1389−1395.
(67) Gadre, S. R.; Suresh, C. H.; Mohan, N. Electrostatic potential topology for probing molecular structure, bonding and reactivity. *Molecules* **2021**, *26*, 3289.
(68) Kumar, P. S. V.; Raghavendra, V.; Subramanian, V. Bader's theory of atoms in molecules (AIM) and its applications to chemical bonding. *J. Chem. Sci.* **2016**, *128*, 1527−1536.
(69) Hajji, M.; Abad, N.; Habib, M. A.; Elmgirhi, S. M. H.; Guerfel, T. Computational chemistry methods for modelling non-covalent interactions and chemical reactivity-An overview. *J. Indian Chem. Soc.* **2021**, *98*, No. 100208.
(70) Kramer, C. A. C.; da Silva, A. R. L.; de Lima-Neto, P.; de Carvalho, L. S. Computational approach in lignin structural models: Influence of non-covalent intramolecular interactions on βO4 bond properties. *J. Mol. Struct.* **2022**, *1251*, No. 131938.
(71) Nagy, Á. Spherical potential functional theory. *J. Chem. Phys.* **2021**, *155*, No. 144108.
(72) Popelier, P. L. A. The QTAIM perspective of chemical bonding. *The Chemical Bond*, Wiley: 2014; *1*, 271−308.
(73) Zhang, J.; Dolg, M. ABCluster: the artificial bee colony algorithm for cluster global optimization. *Phys. Chem. Chem. Phys.* **2015**, *17*, 24173−24181.
(74) Zhang, J.; Dolg, M. Global optimization of clusters of rigid molecules using the artificial bee colony algorithm. *Phys. Chem. Chem. Phys.* **2016**, *18*, 3003−3010.
(75) Baei, M. T.; Peyghan, A. A.; Bagheri, Z. First principles study on encapsulation of alkali metals into ZnO nanocage. *Chin. J. Chem. Phys.* **2012**, *25*, 671−675.
(76) Janjua, M. R. S. A. Prediction and Understanding: Quantum Chemical Framework of Transition Metals Enclosed in a B12N12 Inorganic Nanocluster for Adsorption and Removal of DDT from the Environment. *Inorg. Chem.* **2021**, *60*, 10837−10847.
(77) Bulat, F. A.; Murray, J. S.; Politzer, P. Identifying the most energetic electrons in a molecule: The highest occupied molecular orbital and the average local ionization energy. *Comput. Theor. Chem.* **2021**, *1199*, No. 113192.
(78) Vishwakarma, K.; Rani, S.; Chahal, S.; Lu, C.-Y.; Ray, S. J.; Yang, C.-S.; Kumar, P. Quantum coupled borophene based heterolayers for excitonic and molecular sensing applications. *Phys. Chem. Chem. Phys.* **2022**, *24*, 12816−12826.
(79) Doust Mohammadi, M.; Abdullah, H. Y. Vinyl chloride adsorption onto the surface of pristine, Al-, and Ga-doped boron nitride nanotube: A DFT study. *Solid State Commun.* **2021**, *337*, No. 114440.
(80) Levy, M.; Perdew, J. P.; Sahni, V. Exact differential equation for the density and ionization energy of a many-particle system. *Phys. Rev. A* **1984**, *30*, No. 2745.
(81) Parr, R. G.; Yang, W. Density functional approach to the frontier-electron theory of chemical reactivity. *J. Am. Chem. Soc.* **1984**, *106*, 4049−4050.
(82) Koopmans, T. Über die Zuordnung von Wellenfunktionen und Eigenwerten zu den einzelnen Elektronen eines Atoms. *Physica* **1934**, *1*, 104−113.
(83) Janak, J. F. Proof that $\partial E \partial n_i = \varepsilon$ in density-functional theory. *Phys. Rev. B: Condens. Matter Mater. Phys.* **1978**, *18*, No. 7165.
(84) Narth, C.; Maroun, Z.; Boto, R. A.; Chaudret, R.; Bonnet, M.-L.; Piquemal, J.-P.; Contreras-García, J. A complete NCI perspective: from new bonds to reactivity. In *Applications of Topological Methods in Molecular Chemistry*; Springer, 2016; pp 491−527.

https://doi.org/10.1021/acsomega.3c01177
ACS Omega 2023, 8, 20621−20633